Letter

Gate-defined superconducting channel in magic-angle twisted bilayer graphene

Giulia Zheng ,[1] Elías Portolés ,[1] Alexandra Mestre-Torà ,[1] Marta Perego ,[1] Takashi Taniguchi ,[2] Kenji Watanabe ,[3] Peter Rickhaus ,[1] Folkert K. de Vries ,[1] Thomas Ihn ,[1,4] Klaus Ensslin ,[1,4] and Shuichi Iwakiri [1,*]

[1]Laboratory for Solid State Physics, ETH Zurich, CH-8093 Zurich, Switzerland

[2]Research Center for Materials Nanoarchitectonics, National Institute for Materials Science, 1-1 Namiki, Tsukuba 305-0044, Japan

[3]Research Center for Electronic and Optical Materials, National Institute for Materials Science, 1-1 Namiki, Tsukuba 305-0044, Japan

[4]Quantum Center, ETH Zurich, CH-8093 Zurich, Switzerland

(Received 18 December 2023; revised 17 January 2024; accepted 29 January 2024; published 6 March 2024)

Magic-angle twisted bilayer graphene (MATBG) combines in one single material different phases such as insulating, metallic, and superconducting. These phases and their *in situ* tunability make MATBG an important platform for the fabrication of superconducting devices. We realize a split-gate-defined geometry which enables us to tune the width of a superconducting channel formed in MATBG. We observe a smooth transition from superconductivity to highly resistive transport by progressively reducing the channel width using the split gates or by reducing the density in the channel. Using the gate-defined constriction, we control the flow of the supercurrent, either guiding it through the constriction or throughout the whole device or even blocking its passage completely. This serves as a foundation for developing quantum constriction devices such as superconducting quantum point contacts, quantum dots, and Cooper-pair boxes in MATBG.

DOI: 10.1103/PhysRevResearch.6.L012051

Introduction. Magic-angle twisted bilayer graphene (MATBG) offers highly tunable quantum states [1,2], which have enabled a novel class of gate-defined superconducting nanodevices such as Josephson junctions [3–5], superconducting quantum interference devices (SQUIDs) [6], and ring geometries showing Little-Parks oscillations [7]. All these devices rely on defining interfaces between resistive and superconducting phases. In a gate-defined narrow MATBG constriction, the interface between the superconducting and resistive phases can be continuously controlled and studied. In Bernal bilayer graphene, a constriction (e.g., a quantum point contact [8,9]) can be formed due to its gate-tunable band gap of a few 100 meV [10,11]. However, in the case of MATBG, the size of the band gap between the flat band and the dispersive band is one order of magnitude smaller [4]. Therefore it is challenging to form a similar constriction and the question arises, whether it is possible at all to realize a narrow superconducting channel by tuning the width of confining resistive states.

In this Letter, we demonstrate a gate-defined superconducting channel in MATBG. We observe a smooth transition from supercurrent to highly resistive transport (pinch-off) by progressively reducing the channel width using split gates or by reducing the density in the channel using the channel gate. We find that the supercurrent in the constriction can be turned on and off. These results will serve as the foundation for developing constriction-based devices such as superconducting quantum point contacts, quantum dots, or Cooper-pair boxes in MATBG.

Device and bulk characterization. The fabrication starts by encapsulating MATBG (light green) between two hexagonal boron nitride (hBN) layers of thickness 59 and 61 nm (dark green). Additionally, a graphite layer (dark gray) is picked up, serving as the back gate. The lateral device layout is shown in Fig. 1(a). To form electric contacts (orange in the figure), we etch the top hBN using reactive ion etching (RIE) and evaporate Cr(5 nm)/Au(65 nm). On top of the top hBN, we evaporate Cr(5 nm)/Au(15 nm) split gates (blue) with a gap of 150 nm. After depositing a 40-nm layer of aluminum oxide, an additional channel gate (yellow) with a width of 400 nm (in the direction of current flow) is deposited, covering the region in between the split gates. Our gate configuration defines three different areas in the MATBG mesa: The leads shown in light green and tuned only by the back gate, the split-gated region in blue, tuned by split gates and the back gate combined, and the channel in between the split gates and below the channel gate. Since the thickness of the top hBN (59 nm) is comparable to the lateral dimension of the split gate (150 nm), the channel region is tuned not only by the channel gate and the back gate, but also by the split gates due to fringe fields. We perform two-terminal transport measurements at a temperature of 24 mK.

To characterize the twist angle between the graphene layers of the sample, we apply a dc current ($I = 10$ nA) and measure the resulting voltage drop V. We sweep the back-gate voltage V_{bg} while keeping the split-gate voltage V_{sg} and the channel-gate voltage V_{cg} at zero, thus probing the bulk (leads, split-gated region, and channel together). The resulting resistance $R = V/I$ is shown in Fig. 1(b), exhibiting several peaks originating from different filling factors ν of the moiré unit cell. The peak at around $V_{bg} = 0$ indicates charge

*siwakiri@phys.ethz.ch

Published by the American Physical Society under the terms of the Creative Commons Attribution 4.0 International license. Further distribution of this work must maintain attribution to the author(s) and the published article's title, journal citation, and DOI.

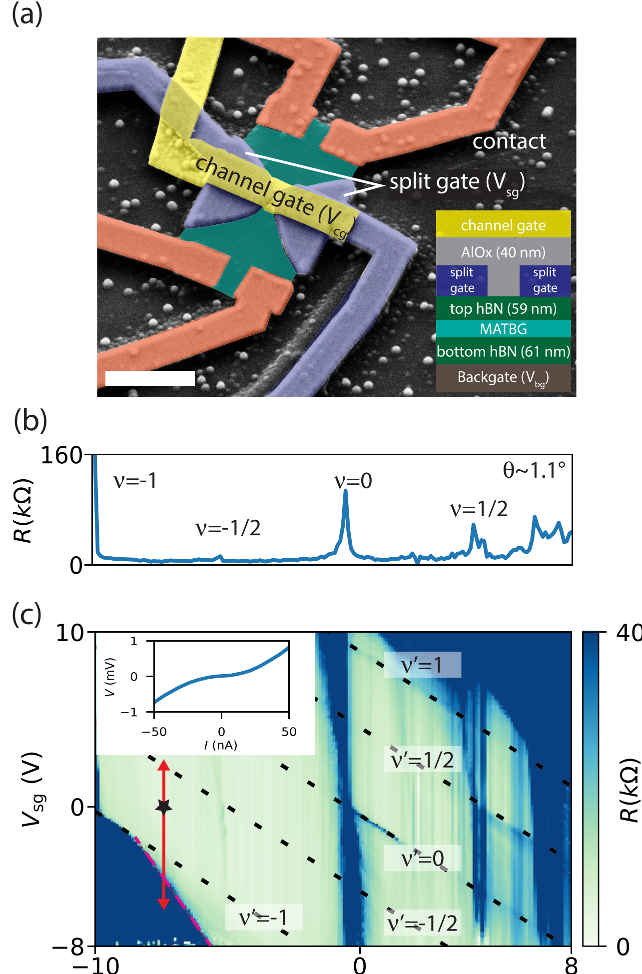

FIG. 1. (a) False-colored scanning electron microscopy (SEM) picture of the sample. The white scale bar at the bottom left indicates 1 µm. MATBG (light green), contacts (orange), split gates (blue), and a channel gate (yellow) are shown. Inset: Schematic of the stack (thickness not to scale). (b) Characterization of the device with $V_{cg} = 0$. Line cut at $V_{sg} = 0$ with annotations of filling factor $\nu = -1$, $-1/2$, 0, 1/2, and 1 states. (c) Mapping of the resistance as a function of V_{sg} and V_{bg}. Black dashed lines labeled $\nu' = -1$, $-1/2$, 0, 1/2 indicate filling factors in the split-gated area. The pink dashed line highlights the transition from low to high resistance in the hole side. The inset shows the superconducting current-voltage characteristic taken at $V_{sg} = 0$ and $V_{bg} = -7.44$ V (indicated by a black star). The red double-sided arrow is the gate voltage range in which Fig. 2(a) is taken.

neutrality ($\nu = 0$). At negative V_{bg}, we observe full-filling ($\nu = -1$, where the Fermi level moves into the dispersive band overcoming a small band gap) and half-filling ($\nu = -1/2$) peaks for holes. At positive voltages we observe half filling ($\nu = 1/2$) for electrons, where the Fermi level resides within the flat bands. Superconductivity appears at filling factors slightly larger than 1/2. Filling $\nu = 1$ for electrons cannot be reached due to the voltage range of the back gate being limited by leakage currents. We extract the twist angle between the graphene layers of the device from the density of the $\nu = -1$ peak, which leads to 1.1° (see Appendix A).

To demonstrate the area-selective tunability of moiré filling factors, Fig. 1(c) shows R as a function of V_{sg} and V_{bg}. Filling factors $\nu' = -1$, $-1/2$, 0, 1/2, and 1 below the split gates are indicated with black dashed lines. The inset in Fig. 1(c) shows a typical current-voltage (I-V) characteristic in the superconducting regime at $V_{bg} = -7.44$ V, $V_{sg} = 0$, and $V_{cg} = 0$. Here, a constant contact resistance of 10 kΩ, observed as the offset resistance at zero-bias current in the superconducting regime, is subtracted from the raw data. In the remainder of this Letter, we consider transport to be superconducting when such an I-V characteristic is observed.

A question arising from the map shown in Fig. 1(c) is the origin of the highly resistive area that spans out in the $\nu' < -1$ region (see the blue region delimited by the dashed pink line). In a standard back-gated MATBG without any top gates [1,2], only a resistance peak can be observed as a function of V_{bg} and not a resistive area as a function of V_{bg} and V_{sg}. In addition, at first glance, one would expect the edge of this high resistive area (dashed pink line) to coincide with the predicted $\nu' = -1$ (the labeled dashed black line). The explanation for why this is not the case lies below.

Tunable superconducting channel: Control via split gates. We now study the effect of the split gates on the supercurrent. We tune the leads to the superconducting regime by setting $V_{bg} = -7.44$ V [cf. red arrow in Fig. 1(c)] and keep $V_{cg} = 0$. Figure 2(a) shows the dV/dI characteristics numerically calculated from the measured dc V-I data as a function of the current I and the split-gate voltage V_{sg}. We assign the state of the carrier gas below the split gates as a function of V_{sg} according to Fig. 1(c) and a capacitance model (see Appendix B) as indicated in Fig. 2(a) by the colored bar above the color plot. When $-6\,\text{V} < V_{sg} < -2.8$ V, the filling factor under the split gate is smaller than -1, and thus the carrier gas in the region below the split gates is either a band insulator (BI) or the Fermi energy is in the dispersive band. When the voltage is increased to $V_{sg} > -2.8$ V, the Fermi energy in the region below the split gates is in the flat bands.

In the range $-6\,\text{V} < V_{sg} < -5.5$ V [before the pink dot in Fig. 2(a)], the device shows a large zero-bias resistance of 0.48 MΩ. This can also be seen in the large slope of the I-V characteristic in Fig. 2(b) (black dashed line). Such a high resistance despite superconducting (SC) leads means that not only is the region below the split gates resistive, but the resistive region extends into the channel region between them due to fringe fields.

When the split-gate voltage is increased to $-5.5\,\text{V} < V_{sg} < -2.8$ V [beyond pink dot in Fig. 2(a)], the device shows low resistance at low bias and a nonlinear I-V characteristic reminiscent of a superconductor as shown by the yellow curve in Fig. 2(b). In this regime, the transport characteristic across the sample remains superconducting even though the area below the split gates is resistive. This indicates that a supercurrent flows through the channel while the split-gated region confines the flow. When V_{sg} is increased beyond -2.8 V, the nonlinear transport and the critical currents become more prominent [see green curve in Fig. 2(b)]. In this regime, the supercurrent extends from the channel into the split-gated regions, eventually rendering the entire device superconducting.

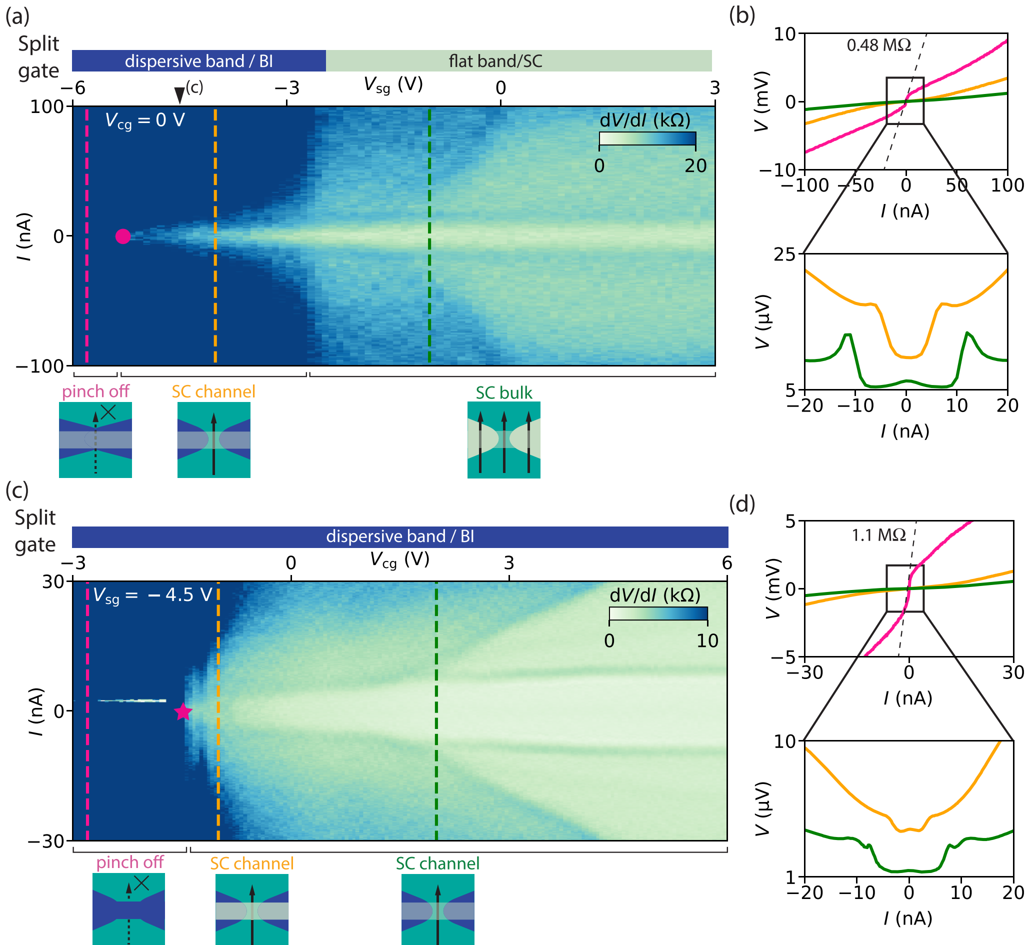

FIG. 2. Differential resistance (dV/dI) as a function of current I and gate voltages. (a) Split gate V_{sg} is swept while keeping $V_{cg} = 0$ V. (b) Voltage drop as a function of dc current and zoom-in picture of dV/dI at $V_{sg} = -5.8$ (pink), -4 (yellow), -1 (green) V. (c) Channel gate V_{cg} is swept while keeping $V_{sg} = -4.5$ V. (d) I-V trace and zoom-in picture of dV/dI at $V_{cg} = -2.8$, -1, and 2 V. The states under the split gate (dispersive band/BI or flat band/SC) are indicated by the bars above the top axes. In all cases, V_{bg} is kept at zero. Pink, yellow, and green dashed vertical lines show the gate voltage at which the line cuts are taken. Illustrations of the device's state (pinch-off, SC channel, or SC bulk) are also shown. Red circle and star symbols show the onset of pinch-off.

Tunable superconducting channel: Control via channel gate. In Figs. 2(c) and 2(d) we show that the conductance of the superconducting channel can also be tuned with the channel-gate voltage. It is only the channel that is tuned by V_{cg} because the metallic split gate screens the electric field of the channel gate. We keep the leads superconducting ($V_{bg} = -7.44$ V) and tune the Fermi energy in the split-gated regions into the dispersive bands ($V_{sg} = -4.5$ V). This corresponds to the condition in Fig. 2(a) indicated by the black triangle on the upper axis.

Under these conditions, we see in Fig. 2(c) at $V_{cg} = 0$ nonlinear transport indicating superconducting behavior consistent with Fig. 2(a). By reducing V_{cg} below -1.5 V, thereby tuning the Fermi energy in the channel towards the BI or the dispersive band, the device exhibits a high resistance of 1.1 MΩ and a nonlinear I-V characteristic with a large slope around zero bias as shown in Fig. 2(d) (black dashed line). This means that the superconducting channel is pinched off. Note that the light green line in Fig. 2(c) is an artifact. When V_{cg} is increased above 0 V, the superconductivity in the channel is enhanced as illustrated by the green curve in Fig. 2(d). The confinement of the superconducting current to the channel and the local gate tunability of the channel from the superconducting to the highly resistive (pinch-off) state of the constriction are the central experimental findings of this Letter.

V_{cg} vs V_{sg} mapping of resistance. To further highlight that the pinch-off in Fig. 2(c) originates from the channel, we show the resistance of the device as a function of V_{sg} and V_{cg} in Fig. 3. Pink symbols indicate the gate voltages at which the channel is pinched off as observed in the data of Figs. 2 and 5 (see Appendix C). These values lie on a line with a negative slope (see the black line in the figure). This means that there exists a regime in which the channel conductance is controlled by both V_{sg} and V_{cg}. This is due to the fringe fields of the split gates, such that the channel conductance is controlled by all three gates. This additionally explains the origin of the discrepancy between the expected $\nu' = 1$ (the labeled dashed black line) and the high resistance edge (dashed pink line) in Fig. 1(c). In between the two dashed lines, the resistance is low because even if the split-gated region is resistive, a supercurrent can still flow through the channel. Only when the

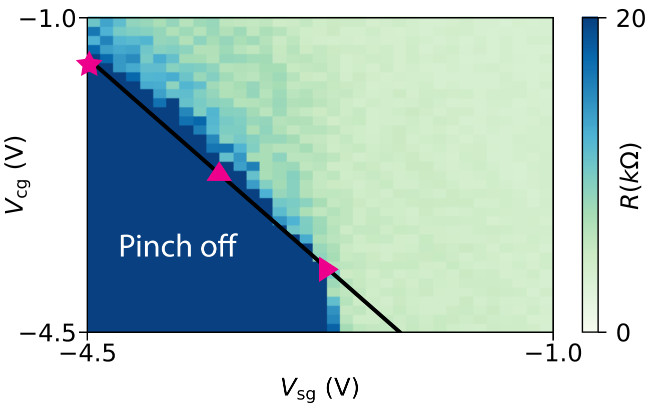

FIG. 3. Mapping of resistance as a function of V_{sg} and V_{cg} at a constant back-gate voltage of $V_{bg} = -7.44$ V. Colored symbols and black line interpolating between them indicate the threshold gate voltages of the pinch-off. The gate-voltage regime where high resistances ($R > 20$ kΩ) are observed is annotated as "Pinch off."

channel is pinched off due to the effect of the fringing fields do we measure a high resistance.

Discussion. In narrow superconducting channels, it has been predicted that the critical current becomes quantized as the channel size is reduced when the BCS coherence length of the superconductor is longer than the channel length [12]. A stepwise change of supercurrent, if not the predicted exact quantization, has been observed in various materials such as InAs [13–16], Ge/Si [17,18], and $SrTiO_3$ [19]. In our device, we did not observe such quantization of the critical current. In MATBG, the BCS coherence length is estimated to be from a few tens of nm up to 100 nm [3,7]. The length of our channel is 400 nm, which is much longer than the estimated coherence length. In order to observe the quantization of the critical current, it is necessary to reduce the channel length down to less than 100 nm, which is possible by advanced electron beam lithography.

Furthermore, we discuss the conditions at which the pinch-off occurs. In Figs. 2(a) and 2(c), the points at which the channel is pinched off are $(V_{bg}, V_{sg}, V_{cg}) = (-7.44, -5.3, 0)$ and $(-7.44, -4.5, -1.5)$ V, respectively. Using the capacitance model (see Appendix B), we estimate the corresponding

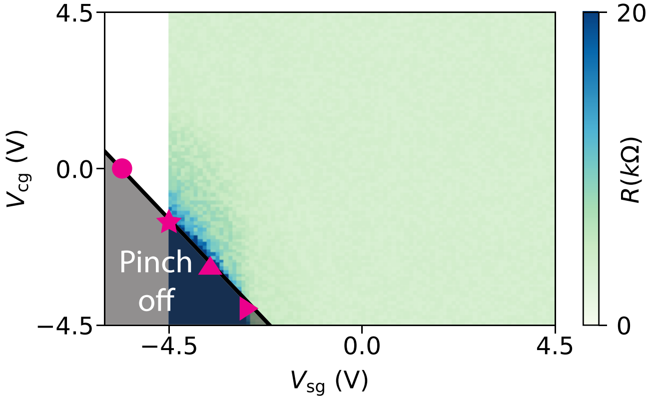

FIG. 4. Resistance as a function of V_{sg} and V_{cg}. at a constant back-gate voltage of $V_{bg} = -7.44$ V with an extended plot area.

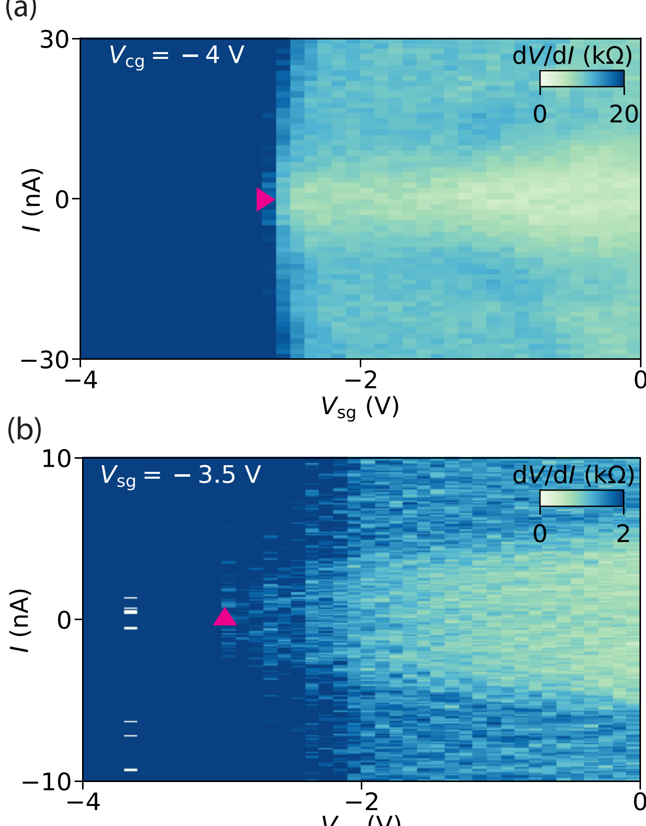

FIG. 5. dV/dI as a function of V_{sg} with fixed $V_{bg} = -7.44$ V and $V_{cg} = -4$ V. Here, the pinch-off of the channel is observed at $V_{sg} = -2.7$ V (see the pink rotated triangular symbol). (b) shows dV/dI as a function of V_{cg} with fixed $V_{bg} = -7.44$ V and $V_{sg} = -3.5$ V.

carrier densities n_{ch} in the channel to be -2.23×10^{12} cm^{-2} and -2.56×10^{12} cm^{-2}. For simplicity, we do not take fringe field effects into account in the model. By assuming an isotropic Fermi surface and fourfold degeneracy, the corresponding Fermi wavelengths $\lambda_F = 2\sqrt{\pi/|n_{ch}|}$ are 23.7 and 22.1 nm, respectively. Therefore, one can estimate the minimal width of the channel that supports normal conducting transport to be around this value (∼20 nm), which is significantly smaller than its lithographic value (150 nm). Moreover, in this narrow-channel limit, one can expect conductance quantization in the normal conducting regime. However, we did not observe any signature of normal conductance quantization, presumably due to disorder and the relatively low resistance of the insulating state in MATBG (∼1 MΩ in this device) compared to gapped Bernal bilayer graphene (∼100 MΩ [20]). Nevertheless, the superconducting channel can be formed as long as its resistance, which is ideally zero, is low enough compared to the resistance of the split-gated area.

Conclusion. We have realized a gate-defined superconducting channel in MATBG by implementing a device with a back gate and two layers of top gates (split gates and a channel gate). We observe a transition from superconducting to highly resistive (up to ∼1 MΩ) transport through the channel by tuning the split-gate and channel-gate voltages.

This shows that it is possible to define a narrow superconducting channel by tuning the width of the confining resistive areas. The threshold at which the pinch-off occurs depends not only on the channel gate but also on the split-gate voltage, indicating the essential role of the fringe field effects. Our findings serve as a foundation for developing quantum constriction devices such as superconducting quantum point contacts, quantum dots, and Cooper-pair boxes in MATBG.

Acknowledgments. We are grateful for fruitful discussions and technical support from P. Maerki, T. Baehler, R. Garreis, C. Tong, B. Kratochwil, W. Huang, and the ETH FIRST cleanroom facility staff. We acknowledge financial support by the European Graphene Flagship Core3 Project, H2020 European Research Council (ERC) Synergy Grant under Grant Agreement No. 951541, the European Union's Horizon 2020 research and innovation program under Grant Agreement No. 862660/QUANTUM E LEAPS, the European Innovation Council under Grant Agreement No. 101046231/FantastiCOF, and NCCR QSIT (Swiss National Science Foundation, Grant No. 51NF40-185902). K.W. and T.T. acknowledge support from the JSPS KAKENHI (Grants No. 21H05233 and No. 23H02052) and World Premier International Research Center Initiative (WPI), Ministry of Education, Culture, Sports, Science and Technology (MEXT), Japan. E.P. acknowledges support of a fellowship from "la Caixa" Foundation (ID 100010434) under fellowship code LCF/BQ/EU19/11710062.

Appendix A: Extraction of twist angle. We extract the twist angle of the sample using the relation $\theta = 2\arcsin(\frac{a}{2L})$. Here, a is the lattice constant of graphene, and L is the moiré periodicity, representing the distance between two AA-stacked regions. L is related to the area $\mathcal{A}$ of the moiré unit cell via $L = 2\sqrt{2\mathcal{A}/\sqrt{3}}$. A moiré unit cell can host four electrons due to spin and valley degeneracy. Using this, the full filling resistance peak appears at the density that corresponds to the occupation of four electrons per moiré unit cell $\mathcal{A} = \frac{4}{n_{\nu=1}}$.

Appendix B: Capacitance Model. To estimate the carrier density in the device, we estimate the capacitance per unit area of the back gate, split gate, and channel gate to be $C_{\mathrm{bg}} = \varepsilon_0\varepsilon_{\mathrm{hBN}}/d_{\mathrm{bot}}$, $C_{\mathrm{sg}} = \varepsilon_0\varepsilon_{\mathrm{hBN}}/d_{\mathrm{top}}$, and $C_{\mathrm{cg}} = \varepsilon_0\varepsilon_{\mathrm{hBN}}\varepsilon_{\mathrm{AlOx}}/(\varepsilon_{\mathrm{hBN}}d_{\mathrm{top}} + \varepsilon_{\mathrm{AlOx}}d_{\mathrm{AlOx}})$. Here, $\varepsilon_0 = 8.854 \times 10^{-12}$ is the vacuum permittivity, $\varepsilon_{\mathrm{hBN}} = 3.3$ and $\varepsilon_{\mathrm{AlOx}} = 9.5$ are the relative permittivities of the hBN and the aluminum oxide, d_{top} and d_{bot} are the thicknesses of the top and bottom hBN, and d_{AlOx} is the thickness of the aluminum oxide layer. We then calculate the carrier density of the lead as $n_{\mathrm{bg}} = C_{\mathrm{bg}}V_{\mathrm{bg}}/e$, the region below the split gate as $n_{\mathrm{sg}} = (C_{\mathrm{bg}}V_{\mathrm{bg}} + C_{\mathrm{sg}}V_{\mathrm{sg}})/e$, and the region below the channel gate as $n_{\mathrm{cg}} = (C_{\mathrm{bg}}V_{\mathrm{bg}} + C_{\mathrm{cg}}V_{\mathrm{cg}})/e$, where e is the elementary charge.

Appendix C: Extended map of $R(V_{cg}, V_{sg})$. The same map as Fig. 3 but with an extended range is shown in Fig. 4. The threshold for pinch-off extracted from the I-V characteristic measurements are plotted as symbols. Even though the data cannot be measured due to the leakage of the gate that happened at the last stage of the entire experiment, one can clearly see the linear relation between the threshold value of V_{cg} and V_{sg}.

Appendix D: Extended map for $dV/dI(I, V_{\mathrm{cg}})$ and $dV/dI(I, V_{\mathrm{sg}})$. We measure the behavior of the superconducting channel in the same manner as in Fig. 2 but in two more configurations as shown in Fig. 5. In Fig. 5(a), V_{sg} is swept with fixed $V_{\mathrm{bg}} = -7.44$ V and $V_{\mathrm{cg}} = -4$ V. Here, the pinch-off of the channel is observed at $V_{\mathrm{sg}} = -2.7$ V (see the pink rotated triangular symbol). In Fig. 5(b), V_{cg} is swept with fixed $V_{\mathrm{bg}} = -7.44$ V and $V_{\mathrm{sg}} = -3.5$ V. Here, the pinch-off of the channel is observed at $V_{\mathrm{cg}} = -2.88$ V (see the pink rotated triangular symbol). These points are plotted in Figs. 3 and 4.

[1] Y. Cao, V. Fatemi, S. Fang, K. Watanabe, T. Taniguchi, E. Kaxiras, and P. Jarillo-Herrero, Unconventional superconductivity in magic-angle graphene superlattices, Nature (London) **556**, 43 (2018).

[2] M. Yankowitz, S. Chen, H. Polshyn, Y. Zhang, K. Watanabe, T. Taniguchi, D. Graf, A. F. Young, and C. R. Dean, Tuning superconductivity in twisted bilayer graphene, Science **363**, 1059 (2019).

[3] F. K. de Vries, E. Portolés, G. Zheng, T. Taniguchi, K. Watanabe, T. Ihn, K. Ensslin, and P. Rickhaus, Gate-defined Josephson junctions in magic-angle twisted bilayer graphene, Nat. Nanotechnol. **16**, 760 (2021).

[4] D. Rodan-Legrain, Y. Cao, J. M. Park, S. C. de la Barrera, M. T. Randeria, K. Watanabe, T. Taniguchi, and P. Jarillo-Herrero, Highly tunable junctions and non-local Josephson effect in magic-angle graphene tunneling devices, Nat. Nanotechnol. **16**, 769 (2021).

[5] J. Díez-Mérida, A. Díez-Carlón, S. Y. Yang, Y.-M. Xie, X.-J. Gao, J. Senior, K. Watanabe, T. Taniguchi, X. Lu, A. P. Higginbotham, K. T. Law, and Dmitri K. Efetov, Symmetry-broken Josephson junctions and superconducting diodes in magic-angle twisted bilayer graphene, Nat. Commun. **14**, 2396 (2023).

[6] E. Portolés, S. Iwakiri, G. Zheng, P. Rickhaus, T. Taniguchi, K. Watanabe, T. Ihn, K. Ensslin, and F. K. de Vries, A tunable monolithic squid in twisted bilayer graphene, Nat. Nanotechnol. **17**, 1159 (2022).

[7] S. Iwakiri, A. Mestre-Torà, E. Portolés, M. Visscher, M. Perego, G. Zheng, T. Taniguchi, K. Watanabe, M. Sigrist, T. Ihn, and K. Ensslin, Tunable quantum interferometer for correlated moiré electrons, Nat. Commun. **15**, 390 (2024).

[8] H. Overweg, H. Eggimann, X. Chen, S. Slizovskiy, M. Eich, R. Pisoni, Y. Lee, P. Rickhaus, K. Watanabe, T. Taniguchi, V. Fal'ko, T. Ihn, and K. Ensslin, Electrostatically induced quantum point contacts in bilayer graphene, Nano Lett. **18**, 553 (2018).

[9] S. Nakaharai, J. R. Williams, and C. M. Marcus, Gate-defined graphene quantum point contact in the quantum Hall regime, Phys. Rev. Lett. **107**, 036602 (2011).

[10] T. Ohta, A. Bostwick, T. Seyller, K. Horn, and E. Rotenberg, Controlling the electronic structure of bilayer graphene, Science **313**, 951 (2006).

[11] J. B. Oostinga, H. B. Heersche, X. Liu, A. F. Morpurgo, and L. M. K. Vandersypen, Gate-induced insulating state in bilayer graphene devices, Nat. Mater. **7**, 151 (2008).

[12] C. W. Beenakker and H. van Houten, Josephson current through a superconducting quantum point contact shorter than the coherence length, Phys. Rev. Lett. **66**, 3056 (1991).

[13] T. Bauch, E. Hürfeld, V. M. Krasnov, P. Delsing, H. Takayanagi, and T. Akazaki, Correlated quantization of supercurrent and conductance in a superconducting quantum point contact, Phys. Rev. B **71**, 174502 (2005).

[14] S. Abay, D. Persson, H. Nilsson, H Q Xu, M. Fogelström, V. Shumeiko, and P. Delsing, Quantized conductance and its correlation to the supercurrent in a nanowire connected to superconductors, Nano Lett. **13**, 3614 (2013).

[15] H. Irie, Y. Harada, H. Sugiyama, and T. Akazaki, Josephson coupling through one-dimensional ballistic channel in semiconductor-superconductor hybrid quantum point contacts, Phys. Rev. B **89**, 165415 (2014).

[16] H. Takayanagi, T. Akazaki, and J. Nitta, Observation of maximum supercurrent quantization in a superconducting quantum point contact, Phys. Rev. Lett. **75**, 3533 (1995).

[17] J. Xiang, A Vidan, M. Tinkham, R. M. Westervelt, and C. M. Lieber, Ge/Si nanowire mesoscopic Josephson junctions, Nat. Nanotechnol. **1**, 208 (2006).

[18] N. W. Hendrickx, M. L. V. Tagliaferri, M. Kouwenhoven, R. Li, D. P. Franke, A. Sammak, A. Brinkman, G. Scappucci, and M. Veldhorst, Ballistic supercurrent discretization and micrometer-long Josephson coupling in germanium, Phys. Rev. B **99**, 075435 (2019).

[19] E. Mikheev, I. T. Rosen, and D. Goldhaber-Gordon, Quantized critical supercurrent in $SrTiO_3$-based quantum point contacts, Sci. Adv. **7**, eabi6520 (2021).

[20] H. Overweg, Electrostatically induced nanostructures in bilayer graphene, Ph.D. thesis, ETH Zurich, 2018, https://doi.org/10.3929/ethz-b-000278503.